

Complex denoising of MR data via wavelet analysis: Application for functional MRI

Saleem Zaroubi¹, Gadi Goelman*

*Human Biology Research Center, Department of Medical Biophysics and Nuclear Medicine, Hadassah Hebrew University Hospital, Ein - Karem,
P.O.B 12000, Jerusalem 91120, Israel*

Received 19 January 1999; accepted 7 August 1999

Abstract

A fast post-processing method for noise reduction of MR images, termed complex-denoising, is presented. The method is based on shrinking noisy discrete wavelet transform coefficients via thresholding, and it can be used for any MRI data-set with no need for high power computers. Unlike previous wavelet application to MR images, the denoising algorithm is applied, separately, to the two orthogonal sets of the complex MR image. The norm of the combined data are used to construct the image. With this method, signal-noise decoupling and Gaussian white noise assumptions used in the wavelet noise suppression scheme, are better fulfilled. The performance of the method is tested by carrying out a qualitative and quantitative comparison of a single-average image, complex-denoised image, multiple-average images, and a magnitude-denoised image, of a standard phantom. The comparison shows that the complex-denoising scheme improves the signal-to-noise and contrast-to-noise ratios more than the magnitude-denoising scheme, particularly in low SNR regions. To demonstrate the method strength, it is applied to fMRI data of somatosensory rat stimulation. It is shown that the activation area in a cross-correlation analysis is ~63% larger in the complex-denoised versus original data sets when equal threshold value is used. Application of the method of Principal Component Analysis to the complex-denoised, magnitude-denoised, and original data sets results in a similar but higher variance of the first few principal components obtained from the former data set as compared to those obtained from the later two sets. © 2000 Elsevier Science Inc. All rights reserved.

Keywords: Wavelet; Denoising; fMRI

1. Introduction

Functional magnetic resonance imaging (fMRI) techniques are being used to obtain information on human brain neuronal activity [1–10]. These techniques provide high spatial and temporal resolution and allow longitudinal studies because some are completely non-invasive. The success of these techniques to determine functional sites of various tasks made fMRI a center tool in neuro-imaging. To increase temporal resolution, echo planar imaging (EPI) and/or fast gradient recall echo techniques are used resulting in low signal-to-noise ratio (SNR) images. Therefore, major effort is made recently to suppress noise in fMRI [11].

In this paper, we present a nonlinear denoising algorithm

based on wavelet analysis that suppress the Gaussian white noise. This method, based on an existing technique, is modified to be especially suited to MRI. It is shown that, in MRI, the modified wavelet denoising algorithm is superior to the existing wavelet denoising methods, particularly for low SNR images. Therefore, it is specifically suited to fMRI data-sets.

Several methods to recover an image from its noisy data exist, starting from the classic, e.g., Wiener filtering [12,13] and Principal Component Analysis [14], to the more modern, and usually non-linear, such as Artificial Neural Networks [15], Maximum-Entropy [16], or Wavelets analysis [17–19]. All of these methods attempt, subject to some assumptions, to extract the maximum amount of “useful” information from the data. In many of those methods, the data are expanded in some functional basis that maintains their phase and amplitude distribution. With a clever choice of functional basis, it is often possible to distinguish between the various contributions to the MR data and to filter

* Corresponding author. Tel.: +1-972-2-677-7455; fax: +1-972-2-642-1203.

E-mail address: gadig@hadassah.org.il (G. Goelman)

¹ Current address: Max Planck Institute for Astrophysics, Garching, Germany.

the noise. In this paper, we choose to work with a non-linear denoising scheme in Wavelet space, where Gaussian white noise is especially easy to pick out from the raw data [20–22].

During the last decade, wavelets have become a popular tool in various data analysis and signal and image processing applications. Wavelet functional bases' main appeal stems from their simultaneous localization in both the wave-number (frequency) and the position (time) domains, where they allow for an orthogonal and complete projection on modes localized in both spaces. The localization allows compressing the noiseless data features into a very small number of very large wavelet coefficients. Gaussian white noise, however, stays as white noise in any orthogonal basis, therefore spreading, in wavelet space, over all expansion coefficients and contributes to each of them a relatively small amplitude. Consequently, in wavelet basis, the noiseless signal dominated coefficients can be easily singled out from their noise dominated counterparts [20,21,23].

Application of wavelets for denoising of MR images has been pioneered by Weaver et al. [24] who applied their denoising scheme on MR images of the human neck. They concluded that the denoising scheme can reduce noise from 10 to 50% without reducing edge sharpness. Other than denoising via wavelets [24–27], researchers has found many other wavelet applications to MRI, including wavelet encoding of MR images (e.g., [26,28,29]) and MR data compression (e.g., [30]).

In the above application of wavelet denoising of MRI data, the denoising was performed on the images themselves (we term this method “magnitude denoising”). However, in MRI, the image noise is not Gaussian [31,32]. Rather, the Gaussian noise assumption applies more correctly to each component of the complex MR data separately. In this paper, Daubechies discrete wavelet basis [17] is used to suppress the noise from each of the complex MR data components, separately; the image is then reconstructed from the data components. In this way, the assumption of Gaussian white noise is used for each of the data components. Very recently, this idea was used to show improved noise reduction by using wavelet packet [33]. We show here that the application of complex-wavelet denoising improves the SNR similarly to magnitude-denoising at high SNR and performs better at low SNR images, with high computational efficiency. For that reason, the new denoising algorithm is especially suited to 3D data-sets and fMRI data. We show that activation areas obtained from fMRI complex-denoised data have a higher correlation with the stimulus, compared with the activation areas obtained from the original and magnitude-denoised data-sets.

2. Denoising by wavelets

MR image is viewed as a two dimensional complex set of $N \times N$ observations modeled mathematically, after Fourier transform, as

$$I^{obs} = I + \varepsilon \quad (1)$$

where, $I = I\{I_{x_i, y_i}\}$ represents the underlying real or imaginary part of the complex localized signal at position (x_i, y_i) and $\varepsilon = \{\varepsilon_{x_i, y_i}\}$ is the statistical uncertainty assumed to be Gaussian white noise. The first step in denoising the data are to transform them to wavelet space as $I_{\alpha\beta}^{obs}$ where α and β are two dimensional index vectors, corresponding to wavelet's resolution and location along each dimension. Note that, due to the orthonormality and completeness of the discrete wavelet transform (DWT) functional basis, Gaussian white noise with standard deviation σ in image space stays as such in wavelet space.

To study the noise behavior, it is instructive to construct the data sorted wavelet spectrum (SWS), which is the amplitude list of the wavelet coefficients ranked in decreasing order. In this presentation, coefficients presenting mostly noise have a low amplitude while coefficients presenting mostly data have a high amplitude. Distinguishing between these groups is easy. Typical behaviors of the real, imaginary and magnitude values of MR image are shown in Fig. 1. Inspection of the log-log plot of the SWS of the real and imaginary parts of the data (solid lines in Figs. 1b and 1c) reveals two distinct regions, the first consists of a modest decline in the high amplitude region of the spectrum, that breaks sharply into a lower amplitude region where the wavelet coefficients are dominated by the white noise. The break ‘level’ is in accordance with the standard deviation of the image background noise $\sim 10^4$. This demonstrates that, in MRI, one does not need to construct the SWS. Instead, it is sufficient to calculate the standard deviation of the background noise and to use it to define the threshold of the noise dominate region. In other words, one expects the break to approximately occurs at wavelets coefficients with $SNR \sim 1$, namely, approximately at twice the standard deviation of the background noise, as indeed it is the case here.

Having identified the onset of noise dominated regime, one then attempts to obtain an unbiased noise-free estimator of the signal in the wavelet domain,

$$\hat{I}_{\alpha\beta} = \hat{I}_{\alpha\beta}(I_{\alpha\beta}^{obs}, \lambda) \quad (2)$$

where λ is a pre-determined parameter. Donoho [34] and Donoho & Johnstone [21,23] proposed the “soft” thresholding estimator

$$\hat{I}_{\alpha\beta} = \text{sign}(I_{\alpha\beta}^{obs})(|I_{\alpha\beta}^{obs}| - \lambda)_+ \quad (3)$$

which ‘kills’ noise prevalent coefficients and keeps, with λ reduction, ‘true’ signal dominated wavelet coefficients. The constancy of Gaussian white noise power spectrum over all resolution scales makes of the soft thresholding rule (Eq. [3]) an ideal estimator. Since the measurement modeling assumed in Eq. [1] and the normal white noise assumption holds in the real and imaginary parts of the data separately, one has to apply the denoising algorithm to each of them separately. For the magnitude image, both assumptions are not valid. Due to the signal-noise coupling in the data

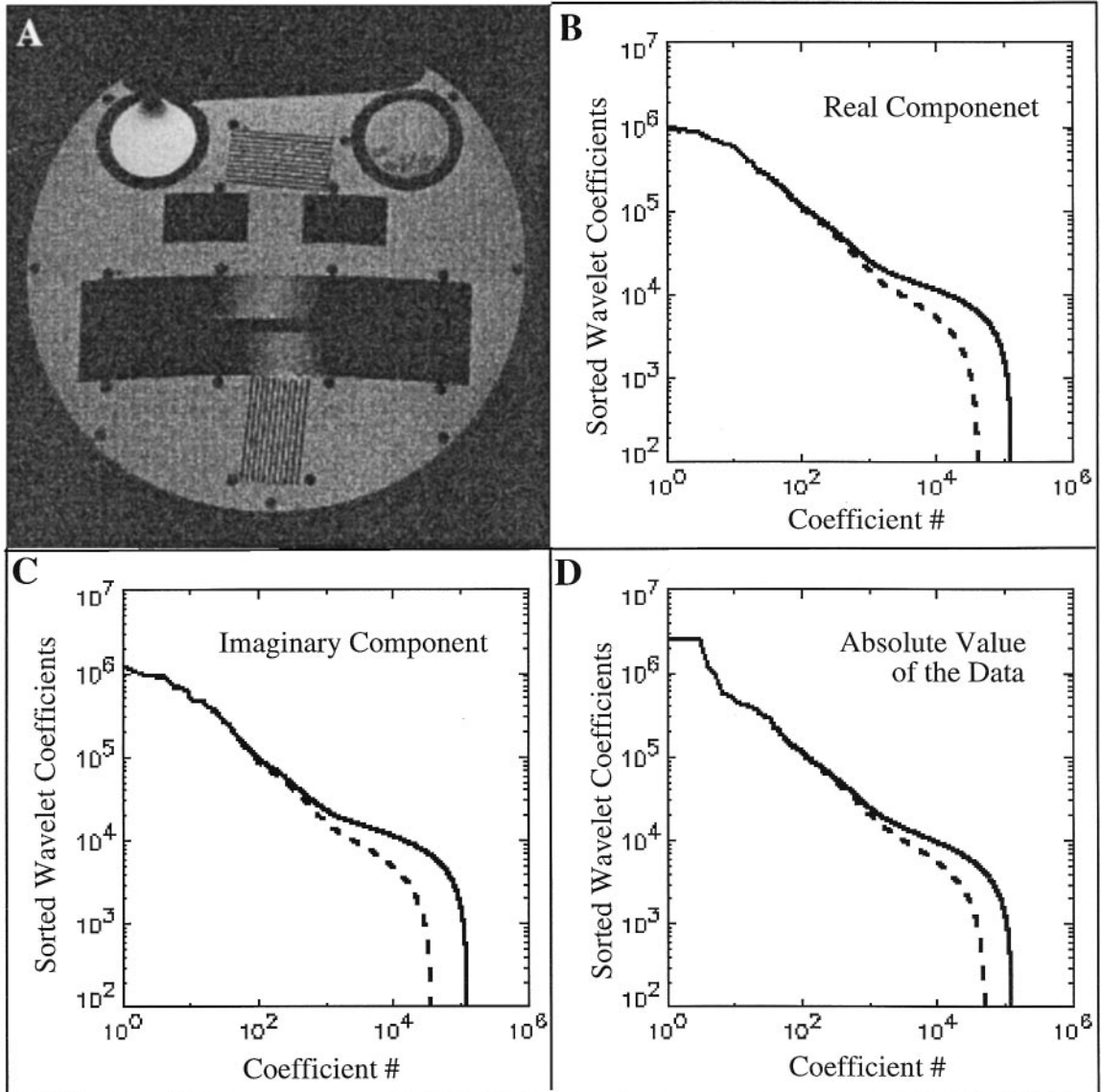


Fig. 1. Illustration of the wavelet denoising algorithm. Panel (a) shows a noisy MR image of a phantom sample used in Table 1. In (b) a sorted wavelet spectrum (SWS), which is the wavelet coefficients ranked in decreasing order, of the real component of the data in A, before (solid line) and after (dashed line) thresholding; (c) the same as in B, but for the imaginary component of the data; and (d) the same as in B, but for the image itself (absolute value). The background noise level in B & C is $\sim 10^4$.

magnitude value, it is practically impossible, in this case, to distinguish noise from signal dominated coefficients. This can be shown by considering a complex datum point $c = (a \pm \varepsilon_1) + i(b \pm \varepsilon_2)$ where ε_1 and ε_2 are the errors in each component. The coupling terms in the datum absolute value,

$$|c| \approx \sqrt{a^2 + b^2 \pm 2a\varepsilon_1 \pm 2b\varepsilon_2 + \varepsilon_1^2 + \varepsilon_2^2} \quad (4)$$

are obvious. This coupling is the main reason for applying the denoising scheme to each of the complex data components separately. In the examples shown in Figs. 1b, 1c, & 1d, the background noise level determines the value of $\lambda = 10^4$. Note however, that for very low SNR ($\ll 1$) Eq. 4 becomes

$$|c| \approx \sqrt{\varepsilon_1^2 + \varepsilon_2^2} \pm \frac{\varepsilon_1 a \pm \varepsilon_2 b}{\sqrt{\varepsilon_1^2 + \varepsilon_2^2}} \quad (5)$$

where for a dominant noise term, say ε_1 , the signal and noise decouple to give the relation $|c| \approx |\varepsilon_1 \pm a|$, which in turn accounts for the break seen in Fig. 1d.

3. Demonstration on a phantom sample

To test the denoising algorithm, we apply it to MR data of a standard phantom sample. The phantom sample consists of a plastic structure filled with several solutions, each

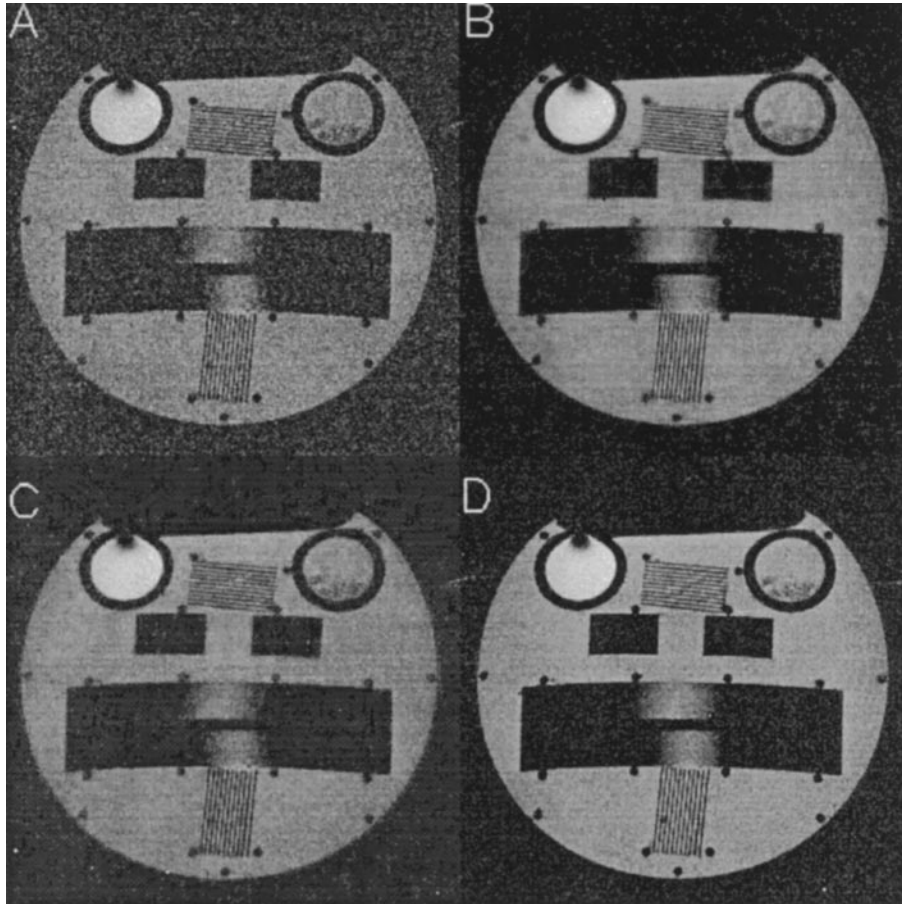


Fig. 2. Comparison of original, complex-denoised, magnitude-denoised and 4-average images. A, the original, single-average, image. B, the image in A after complex denoising. C, the image in A after magnitude denoising. D, the 4-average image. Note the improved contrast-to-noise ratio in B compared to C, the preservation of the sharp transitions between different contrast areas and the high similarity in image quality between the single-average complex-denoised image and the 4-average one.

with different relaxation time. The sample was put in a Bruker-Biospec 4.7T and a 20 cm volume coil was used. MR images were acquired using the fast spin echo technique, with TR of 150 ms, TE_{eff} of 120 ms and matrix size of 512×256 with 2 mm slice width.

Figs. 1b & 1c show the wavelet coefficients ranked in decreasing order (the sorted wavelet spectra) of the real and imaginary components (solid lines). Each of these spectra consists of two distinct regions, corresponding to signal dominated coefficients (high amplitude) and noise dominated coefficients (low amplitude). Independent measurement of the standard deviation of the background shows that it coincides with about half the amplitude of the SWS break-down level (Figs. 1b & c). This supports our denoising approach. The dashed lines in Figs. 1b-d show the sorted wavelet coefficients after 'soft' thresholding (the denoised SWS) used to reconstruct the image in each case (see Fig. 2).

Fig. 2 shows the various reconstructed images. The phantom sample original image is shown in Fig. 2a. The reconstructed image, after denoising the real and the imaginary components separately, termed here after as complex

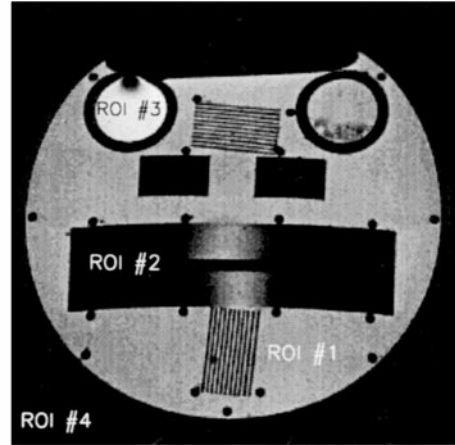
denoising, is shown in Fig. 2b. In this case, note the apparent improvement in SNR and contrast-to-noise ratio (CNR). In Fig. 2c, which is the image obtained after magnitude denoising, there is an improvement in SNR, but the low SNR areas are not fully recovered. For comparison, a 4-average image of the same phantom is also shown (Fig. 2d). An important feature of the wavelet denoising procedure is the retaining of the sharp transitions between areas of different contrasts. This can easily be seen in, for example, the black rings in the image of Fig. 2.

In order to quantify the comparison, we choose several regions of interest (ROIs) on the image (marked on the image attached to Table 1). We then calculate the mean and standard deviation (SD) of those ROIs for each of the original, complex-denoised, magnitude-denoised, 4-average and 22-average images. Beside the expected improvement in the SD, we expect to obtain a better estimate of the means. Since each ROI has a large number of points $<550>$, the mean of the noise in the real and the imaginary parts is approximately zero such that the mean of each ROI equals:

$$mean = \langle |R + \varepsilon_1, I + \varepsilon_2| \rangle \propto \langle R^2 + I^2 + \varepsilon_1^2 + \varepsilon_2^2 \rangle \cong \langle R^2 + I^2 \rangle$$

Table 1
Mean and standard deviation of various regions of interest

Image	ROI			
	1	2	3	4
Original image				
Mean	24223	7622	55651	7227
SD	5692	3827	6036	3802
Complex denoised image				
Mean	22411	2370	53952	2272
SD	1856	1288	2898	1336
Magnitude denoised image				
Mean	21832	6927	54951	6458
SD	2162	1342	3112	1025
4-average image				
Mean	22869	3743	44900	3514
SD	2915	1921	3260	1837
22-average image				
Mean	23519	1371	43654	1373
SD	1120	693	1947	729



and is greater or equal to the ‘true’ mean. This explains why reducing the noise results with lower mean. If we assume that the 22-average image presents the ‘true image’, the closeness between the mean of its ROIs and the denoised image ROIs, can be used as a measure for noise reduction. In the above expression, R and I are the real and imaginary part of the signal, while ε_1 and ε_2 are their noise, correspondingly. In Table 1, we present this comparison. It shows very clearly the superiority of complex-denoising scheme over the magnitude-denoising scheme, where the mean and standard-deviation of the former is closer to those of the 22-average image in all ROIs. For easy observation of this table, we 1) perform F-test to compare variances and 2) compute distances between means. In both tests, we assume that the 22-average is a ‘noise-free’ image and can be used as a gold standard. In the F-test, we take the ratio between the variance of the denoised ROIs and the variance of the 22-average ROIs. The proximity of this ratio to one indicates the extent of noise reduction. The average result of this test for the four different ROIs for the complex-denoised image is 2.91 and 2.98 for the magnitude-denoised image. For comparison, the average result of this test for the original image is 23.28 and 3.87 for the 4-average image. This means that, on average, the SD of both denoised images is lower than the 4-average image, with lower SD for the complex denoised image.

Stronger differences between the complex and magnitude denoised images are observed in the ROI’s means of Table 1. To compare the means, we define the following quantity:

$$\varphi = \frac{|\bar{Y}_{cmplx} - \bar{Y}_{22-avr}|}{|\bar{Y}_{abs} - \bar{Y}_{22-avr}|}$$

where the value of φ presents the ratio between the differences of the ROI’s mean of both denoised images and the 22-average image. For φ equals 1, both denoised images

have equal means, for $\varphi > 1$ the magnitude-denoised means are closer to the 22-average means, while for $\varphi < 1$, the complex-denoised means are closer to the ‘true’ mean. The values obtained for the different ROIs are: $\varphi_1 = 0.652$; $\varphi_2 = 0.18$; $\varphi_3 = 0.91$ and $\varphi_4 = 0.177$, for each ROI respectively. As expected, for high signal-to-noise ratio, (ROI # 3), both methods perform about the same, hence $\varphi \sim 1$. For low signal-to-noise ratio, as in ROI # 2 and 4, the complex-denoised method is performed better resulting with very small φ , and for intermediate SNR, (ROI # 1), φ is intermediate between the two. Note that in all cases $\varphi < 1$, indicating that the mean of the complex-denoised image is closer to the ‘true’ mean.

4. Application to fMRI

4.1. Method

To demonstrate the strength of the method in fMRI, we applied the denoising method to fMRI data of somatosensory stimulation applied on rats. The data were acquired as follows: Male Sprague-Dawley rats (250–350 gr) were anesthetized with urethane i.p. (150 mg/100gr) and put in a Bruker-Biospec 4.7T. The rats’ heads were secured in a home built head holder, body temperature was measured with a rectal thermometer and kept constant by a feedback water blanket. A pair of small needle-electrodes were inserted under the skin of the right or the left hindlimb. The stimulation consisted of 0.3 ms rectangular pulses with frequency of 3Hz and amplitude between 10 to 25 volts. A 20 mm diameter surface coil was used to transmit rf pulses and receive the signal. The surface coil was placed over the skull and centered over the midline of the animal. Coronal slices positioned between bregma 0.5 and –2.5 were taken. MR images were acquired using the gradient echo (GE)

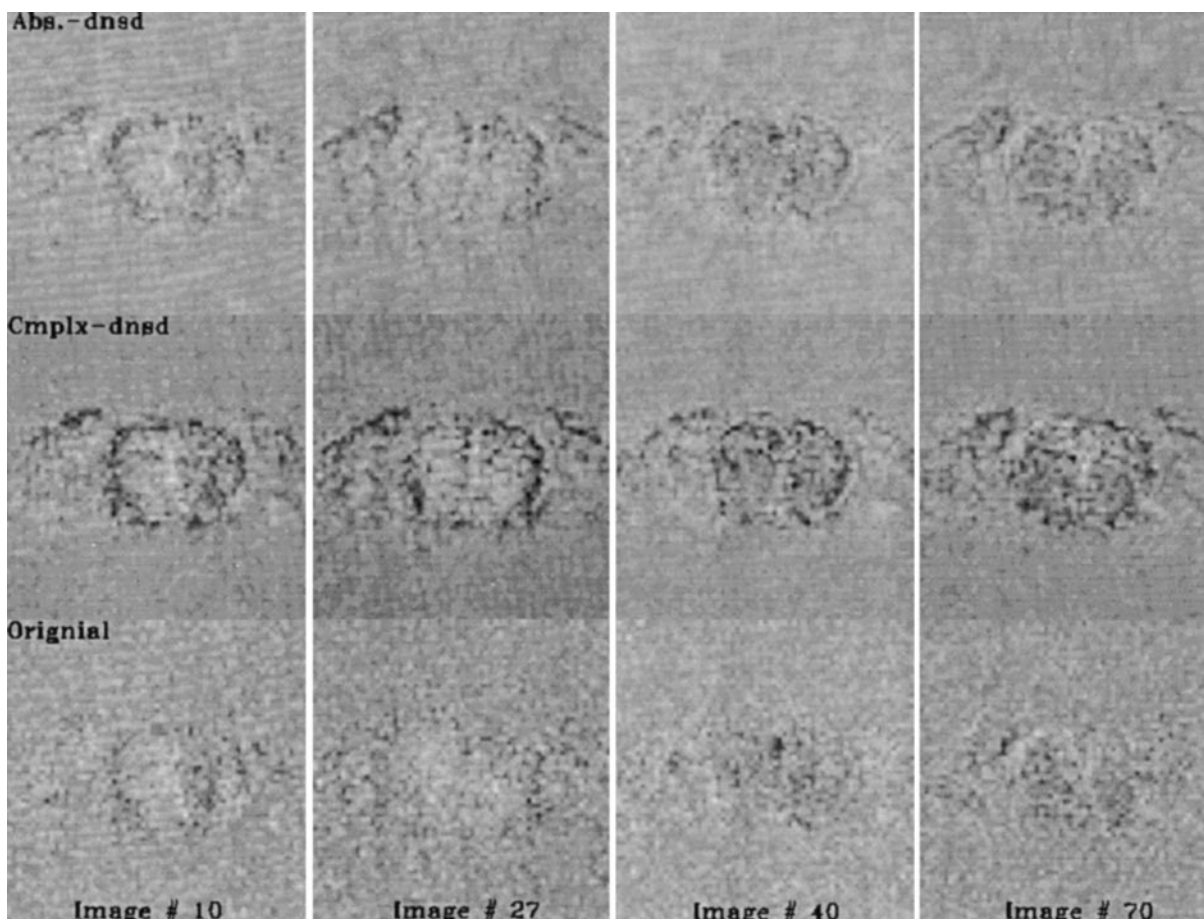


Fig. 3. A comparison of complex and magnitude wavelet denoising algorithm in fMRI data of somatosensory rat stimulation. The bottom row shows four original images, randomly selected from a sequence of 80 images, which were obtained by subtracting the mean image of the time series from each image. The middle row shows the same images after the application of complex denoising and the upper row is the same with application of the magnitude denoising algorithm. Note that the middle row of images has much more details and much higher CNR than the other two.

sequence (TE = 40 ms, TR = 80 ms) with field of view of 2.56 cm, 1 mm slice thickness and 64×64 resolution. The flip angle was $\sim 35^\circ$ in the cortex and lower in deeper structures. Non-periodic 8th order Hadamard matrix rows were used for stimulation in order to avoid any harmony with physiological fluctuations. Two non-periodic rows $[-++-+-]$ and $[-+-+--]$ were used with ‘+’ indicating stimulation on and ‘-’ indicating stimulation off. In each time segment, 10 images were collected (51.2 s) such that each data set contained 80 images and lasted 6.82 min. An interval of at least 15 min was used between successive experiments.

4.2. Data analysis

Image analysis was performed in an external computer using IDL (Interactive Data Language). The denoising algorithm was applied to each of the fMRI data-set in a semi-automatic way as follows: A region in the background is selected from one of the images. The region standard

deviation is calculated and used as the threshold value in the wavelet denoising procedure, performed on the whole set. The denoising algorithm takes ~ 3 s for a single slice of 64×64 resolution on a G3 Mac computer such that the denoising of a data set is quite fast. Two different statistical approaches were used to examine the difference between the complex-denoised, magnitude-denoised and the original data-sets. Our first concern was to show that the denoising algorithm does not change the time-pattern of the data, but only increases its significance by removing the noise. For that purpose, we apply the method of principal component analysis (PCA) to the data. This method searches for the variation in the data and presents it in orthogonal components of decreasing order. PCA was applied to the original, magnitude and complex denoised images and the relevant PCs were compared by their time-pattern appearance and variance. The second method of comparison is the cross-correlation analysis. In this method, each pixel in the data-sets is cross-correlated with the stimulus time course pattern and a correlation map is obtained. A threshold of $C =$

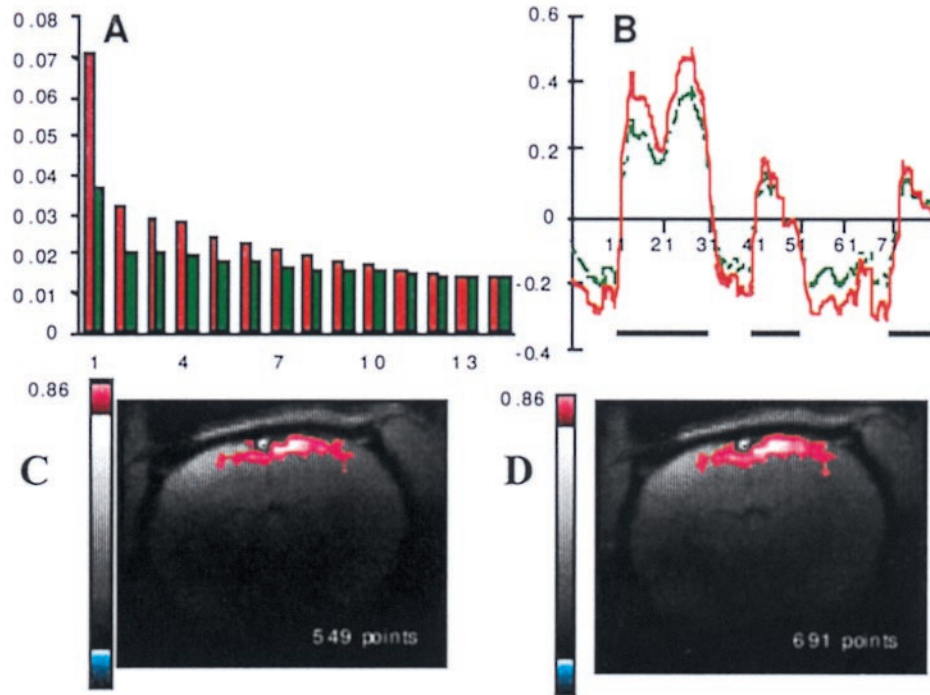


Fig. 4. An fMRI example demonstrating the similarity of activation obtained with the original and complex-denoised sets with higher variance and higher correlation of the later. (a) the variance of the first 14 principal components of the original (green) and complex-denoised (red) sets. The complex wavelet denoising was performed using the image background for the noise threshold as described in the text. On average ($N = 7$), the relevant principal component of the complex-denoised and original sets are different ($p < 0.006$) with 63% higher variance of the former. (b) the first PC for the original (green) and complex-denoised (red) sets. Both PCs have similar time pattern with higher amplitude for the denoised PC. Note the sharp transitions between the stimulation OFF and stimulation ON in both PCs. (c) activation map of the original data. (d) activation map of the data after complex denoising. Original and complex-denoised activation areas are similar with higher area for the complex-denoised set. Note that the location of all extra points in the denoised activation area is inside the brain.

0.35 (sometimes 0.3), corresponding to $p < 0.001$, was used in these maps. The number of pixels above the threshold was calculated and compared.

4.3. Results

Fig. 3 shows the potency of the denoising algorithm when used with fMRI data. Four images, chosen arbitrarily, from one of the fMRI data-sets are shown. Each image is shown after subtracting the mean of the 80 images. The subtraction is imperative, as we are interested in relative changes in the images of the sequence. Note the low SNR of the subtracted images, this SNR makes the new denoising algorithm so efficient. The lower row in Fig. 3 shows the raw images, the second shows the complex-denoised images and the upper row shows the magnitude-denoised images. The improvement introduced to images after both complex-denoising and magnitude denoising schemes is evident. It is also obvious that the contrast to noise ratio (CNR) and SNR is superior in the complex-denoised fMRI data.

In order to use the denoising procedure routinely in fMRI, we have to show that the denoised temporal patterns

are generally similar to the original temporal patterns. This step is crucial since different filtering might modify these patterns leading to wrong results. In Fig. 4, we present an example of such a test. The PCs of the original data (green) and complex denoised data (red) are shown in A. The difference in the variance in the first PC is $\sim 100\%$ and quite high in the other PCs as well. In B, we show the relevant PC (first in this case) for the original and complex denoised data. Relevancy is defined by the PC correlation with the stimulus. As seen, these PCs show temporal patterns that are highly correlated with the stimulus (shown as a boxcar in the bottom of Fig. 4b). It is evident that the PC of the denoised data has a higher amplitude, but also that it retains the general time-activity pattern. Thus, this PC presents stronger changes resulting in higher variance for that pattern. In Fig. 4c & d, we show the activation maps, in color overlaid on B/W reference image. These maps were obtained by cross-correlating the original (Fig. 4c) and the complex-denoised (Fig. 4d) data with the stimulus. As one might expect from the similarity of the PCs, the location of activation is very similar with larger area (691 versus 549 pixels) for the complex-denoised set. Since we do not know a priori what the size of the activation area is, this enlarge-

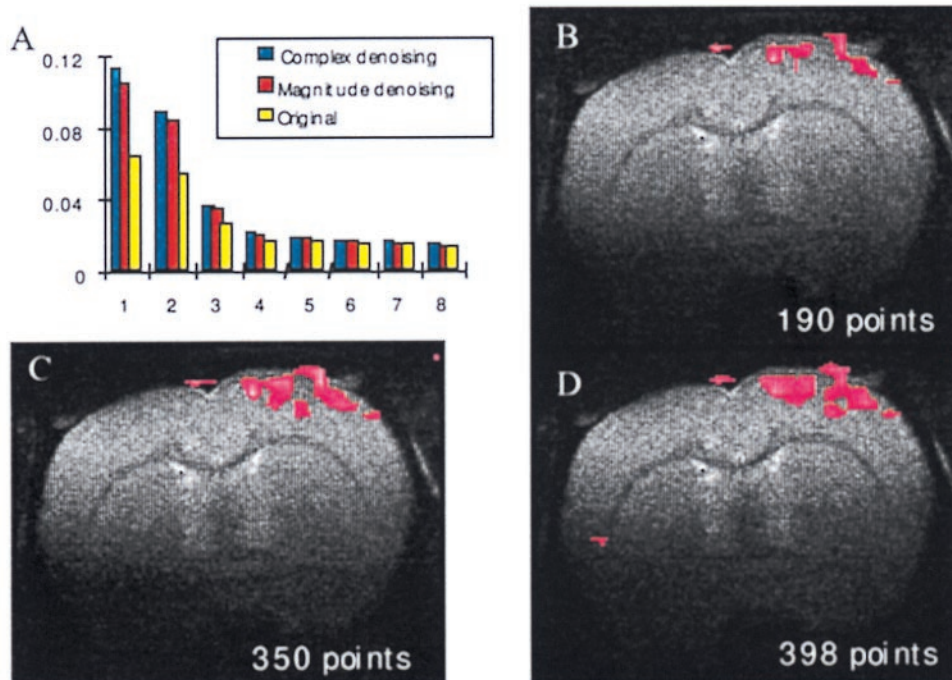


Fig. 5. An example of the difference in principal components and activation maps obtained from the original data, the magnitude-denoised data and the complex-denoised data of somatosensory rat stimulation. The three sets were 1) cross-correlated with the stimulus and 2) analyzed by PCA. (a) the variance of the first eight PCs of the three sets. The variance of the first complex-denoised PC is about twice the variance of the corresponding PC of the original set (11.3% vs. 6.5%) while is little better than the variance of the corresponding PC in the magnitude-denoised set (10.6%). On average, the relevant PC's variance of the complex-denoised set is 63% higher than that of the original set and 26% of the magnitude-denoised set. However, no significant difference was found between the PC's variance of the two denoised sets. (b–d) the activation maps (in red, overlaid on B/W reference images with threshold of .35) including the number of activation pixels, for the original, magnitude-denoised and complex-denoised sets. On average, the activation area of the complex-denoised set is 50% higher than the original (with $p < 0.052$), and 18% higher than the magnitude-denoised set (with $p < 0.023$).

ment might be wrong. However, the similarity of the PCs in particular, the fact that both PCs show the same sharpness of transition from stimulation OFF to stimulation ON, leads us to believe that the difference in activation areas presents real improvement in area definition.

After demonstrating that the denoising algorithm does not modify the time activity pattern, we test the difference between the magnitude and complex wavelet denoising algorithms. In Fig. 5, we show an example of the difference in the principal components and cross-correlation maps obtained with original, complex-denoised and magnitude-denoised data-sets. The variance of the first principal component (PC) in the complex-denoised set is about twice the variance of the corresponding PC in the original set (11.3% vs. 6.5%), while it is a little better than the variance of the corresponding PC in the magnitude-denoised set (10.6%). The other PCs exhibit a similar relation. Using cross-correlation analysis, we obtain a similar pattern: The activation area (correlation above 0.35) is larger in the complex-denoised set (398 pixels), while its size is reduced in the magnitude-denoised set (350 pixels).

To quantify the above, we first check for significant differences in the variance of the PCs and area of activation between the original and the two denoised sets. Second, we

calculated the average percentage of these differences. For the first part, we performed standard t test for matched pairs ($N = 7$) for the relevant (highly correlated with the stimulus) principal components and for the different activation areas. The results of these tests are given in Table 2. As shown in this table, the PC variance of the complex-denoised set is significantly different from the variance of the original PC set, and is 63% higher. However, there is no significant difference between the complex and magnitude denoised PCs although on average, the complex denoised set has a 26% higher variance. The activation area, in the complex-denoised set, is significantly larger than the area of

Table 2
Comparison of the original and denoised fMRI sets in the principal components (PC) and area of activation

	Original vs. magnitude-deno	Original vs. complex-deno	Magnitude- deno vs. complex-deno
Variance of relevant PC and % change	$p = 0.058$ (53)	$p = 0.0058$ (63)	$p = 0.152$ (26)
No. of activation points and % change	$p = 0.075$ (28)	$p = 0.052$ (50)	$p = 0.023$ (18)

the original and magnitude-denoised sets. These improvements justify the use of complex wavelet denoising in fMRI.

5. Conclusion

In this study, we have presented a fast wavelet denoising method for improving MRI quality. The main new idea of this method is that it is applied separately to the two orthogonal components of the MR data. In this way, the basic assumptions used in the denoising algorithm are better satisfied. The difference between the new and magnitude wavelet denoising methods is in low SNR images. We show that, in these cases, the new method suppresses the noise better without deteriorating image quality and with no need for extensive computational efforts.

The strength of the method is demonstrated with fMRI dataset. It was shown that the activation area, defined as the area in which the cross-correlation with the stimulus is above a chosen threshold, is larger in the complex-denoised sets compared with the magnitude-denoised and original data sets. Indeed, we do not know if this larger area presents the ‘true’ activation area better. Inspection of the activation images shows that the extra pixels are either in the cortex or in the sinus vein running perpendicular to the slices. No extra points appear outside the brain. This fact, together with the similarity of the time patterns of the original and denoised PCs, suggests that the denoised activation region defines the ‘true’ activation area in a better way. Another way to look at this is that for the same activation area, the average correlation coefficient in the complex-denoised set, is higher than those obtained for the magnitude-denoised or the original sets.

Due to the new approach’s computational efficiency, it can be used to reduce noise, even further, in a three-dimensional (3D) datasets, where the algorithm is applied to the 3D data set as a whole. It is anticipated that a direct 3D denoising will improve the outcome quality. This is particularly important in fMRI where multiple slices, to cover a large volume of the brain, are routinely acquired.

Acknowledgments

We would like to thank Prof. R. Chisin, Dr. Y. Hoffman and Dr. N. Freedman for their comments on the manuscript. This work was supported by SACTA-RASHI foundation, US-Israel Bi-national Science foundation grant # 95/40 (G.G.) and Israel Ministry of Science grant # 7699–1-95 (G.G.)

References

- [1] Neil JJ. The validation of freely diffusible tracer methods with nuclear magnetic resonance detection for measurement of blood flow. *Magn Reson Med* 1991;19:299–304.
- [2] Ackerman JJ, Ewy C, Becker N, Shalwitz R. Deuterium nuclear magnetic resonance measurements of blood flow and tissue perfusion employing $^2\text{H}_2\text{O}$ as a freely diffusible tracer. *Proc Natl Acad Sci USA* 1987;84:p.4099–102.
- [3] Belliveau JW, Rosen BR, Kantor HL, Rzedzian RR, Kennedy DN, McKinstry RC, Vevea JM, Cohen MS, Pykett IL, Brady TJ. Functional cerebral imaging by susceptibility-contrast NMR. *Magn Reson Med* 1990;14:538.
- [4] Detre JA, Subramanian VH, Mitchell MD, Smith DS, Kobayashi A, Zaman A, Leigh JS. Measurement of regional cerebral blood flow in cat brain using intracarotid $^2\text{H}_2\text{O}$ and ^2H NMR imaging. *Magn Reson Med* 1990;14:389–95.
- [5] Rosen BR, Belliveau JW, Chien D. Perfusion imaging by nuclear magnetic resonance. *Magn Reson Quarterly* 1989;5:263–81.
- [6] Detre JA, Leigh JS, Williams DS, Koretsky AP. Perfusion imaging. *Magn Reson Med* 1992;23:37–45.
- [7] Edelman RR, Mattle HP, Atkinson DJ. Cerebral blood flow: assessment with dynamic contrast-enhanced T_2^* -weighted MR imaging at 1.5 T. *Radiology* 1990;176:211–20.
- [8] Belliveau JW, Kenney DN, Buchbinder RB, Weisskof RM, Cohen MS, Vevea JM, Brady TJ, Rosen BR. Functional mapping of the human visual cortex by magnetic resonance imaging. *Science* 1991; 254:716.
- [9] Ogawa S, Lee TM, Kay AR, Tank DW. Brain magnetic resonance imaging with contrast dependent on blood oxygenation. *Proc Natl Acad Sci USA* 1990;87:9868–72.
- [10] Kwong KK, Belliveau JW, Chester DA, Goldberg IE, Weisskof RM, Poncelet BP, Kennedy DN, Hoppe BE, Cohen MS, Turner R. Dynamic magnetic resonance imaging of human brain activity during primary sensory stimulation. *Proc Natl Acad Sci USA* 1992;89:5675.
- [11] Buonocore MH, Maddock RJ. noise suppression digital filter for functional magnetic resonance imaging based on image reference data. *Magn Reson Med* 1997;38:456–69.
- [12] Wiener N. *Extrapolation and Smoothing of Stationary Time Series*. New York: Wiley, 1949.
- [13] Zaroubi S, Hoffman Y, Fisher KB, Lahav O. Wiener reconstruction of the large scale structure. *Astrophysical J* 1995;449:446–59.
- [14] Jolliffe IT. *Principal Component Analysis*. New York: Springer-Verlag, 1986.
- [15] Hertz J, Krogh A, Palmer RG. *Introduction to the Theory of Neural Computation*. Redwood City, California: Addison-Wesley, 1989.
- [16] Gull SF. Fundamental theories of physics. In: Skilling J, editor. *Maximum Entropy, and Bayesian Methods*. New York: Kluwer, 1989. p. 53.
- [17] Daubechies I. Orthonormal basis of compactly supported wavelets. *Comm Pure Appl Math* 1988;41:909–96.
- [18] Daubechies I. Ten Lectures on Wavelets. In: *CBMS-NSF Regional Conference Series in Applied Mathematics*. Philadelphia, PA, 1992.
- [19] Meyer Y. *Wavelets. Algorithms and Applications*. Philadelphia, PA: SIAM, 1993.
- [20] Mallat SG. A theory for multi-resolution signal decomposition: the wavelet representation. *IEEE Transaction on Pattern Analysis and Machine Intelligence* 1989;11:674–93.
- [21] Donoho DL, Johnstone IM. Ideal spatial adaptation via wavelet shrinkage. *Biometrika* 1994;81:425–55.
- [22] Donoho DL, Johnstone IM. Adapting to unknown smoothness via wavelet shrinkage. *J Am Statist Assoc*, 1996.
- [23] Donoho DL, Johnstone IM. Adapting to unknown smoothness via wavelet shrinkage. *J Am Statist Assoc*, 1994.
- [24] Weaver JB, Xu Y, Healy DM, Cromwell LD. Filtering noise from images with wavelet transforms. *Magn Reson Med* 1991;21:288–95.
- [25] Lu J, Weaver JB, Healy DM, Xu Y. Noise reduction with multiscale edge representation and perceptual criteria. In: *Proceedings of the IEEE-SP International Symposium on Time-Frequency and Time-Scale Analysis*. Victoria, BC, 1992.

- [26] Healy DM, Lu J, Weaver JB. Two applications of wavelets, and related techniques in medical imaging. *Ann Biomed Engineering* 1995;23:637.
- [27] Hilton M, Ogden T, Hattery D, Eden G, Jawerth B. Wavelet denoising in functional MRI data. In: Aldroubi A, Unser M, editors. *Wavelet Application in Biology and Medicine*. Boca Raton, FL: CRC Press, 1996. p. 93–112.
- [28] Weaver JB, Xu Y, Healy DM, Driscoll JR. Wavelet-encoded MR imaging. *Magn Reson Med* 1992;24:265–78.
- [29] Panych LP, Jolesz FA. A dynamically adaptive imaging algorithm for wavelet-encoded MRI. *Magn Reson Med* 1994;32:738–48.
- [30] Maldjian AA, Liu WC, Hirschorn D, Murthy R, Semanczuk W. Wavelet transform based image compression for transmission of MR data. *AJR Am J Roentgenol* 1997;169:23–6.
- [31] Gudbjartsson H, Patz S. The Rician distribution of noisy MRI data. *Magn Reson Med* 1995;34:910–14.
- [32] Macovski A. Noise in MRI. *Magn Reson Med* 1996;36:494–7.
- [33] Wood JC, Johnson KM. wavelet packet denoising of magnetic resonance images: importance of rician noise at low SNR. *Magn Reson Med* 1999;41:631–5.
- [34] Donoho DL. *De-noising Via Soft Thresholding*. Stanford, CT: Stanford University Dept. of Statistics, 1992.